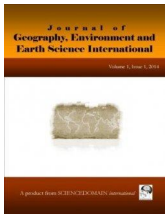

Journal of Geography, Environment and Earth Science International

17(4): 1-19, 2018; Article no.JGEESI.39458
ISSN: 2454-7352

Numerical Dynamic Analysis of the Upper Miocene in the Niger Delta Basin from 3d Seismics

Michael I. Oden[1] and Emmanuel M. Iroka[1*]

[1]Department of Geology, University of Calabar, Calabar, Nigeria.

Author's contributions

This work was carried out in collaboration between the authors. Author MIO designed and wrote the protocol of the study and appraised the data quality. Author EMI managed the literature searches, analyzed the data and wrote the manuscript. Both authors read and approved the final manuscript.

Article Information

DOI: 10.9734/JGEESI/2018/39458
Editor(s):
(1) Dr. Iovine Giulio, CNR-IRPI (National Research Council-Institute of Research for the Geo-hydrologic Protection) of Cosenza, Italy.
(2) Dr. Masum A. Patwary, Academic Ambassador at Large, Geography and Environmental Science, Begum Rokeya University, Bangladesh.
Reviewers:
(1) Joshua Emmanuel Oluwagbemi, University of Ibadan, Nigeria.
(2) Anonymous, Swiss Federal Institute of Technology (ETH), Switzerland.
Complete Peer review History: http://www.sciencedomain.org/review-history/26860

Original Research Article

Received 18 January 2018
Accepted 04 March 2018
Published 25 October 2018

ABSTRACT

Numerical dynamic analysis was carried out for a field in the coastal swamp depobelt of the Niger Delta basin using subsurface growth faults mapped by detailed 3D structural interpretation of seismic data. Orientation analysis of the faults provided the necessary fault plane data while the requisite kinematic information, comprising of slip directions and senses of movement on the faults, were respectively extracted from fault surface corrugations and cut-off points of seismic horizons on the faults. This data set was subjected to paleostress inversion using the rotational optimization module of the Win-tensor program. The results show that the faults are basically dip slip faults with only minor lateral components of displacement. More importantly, it reveals the best-fit paleostress tensor, considered to be active during the Upper Miocene, in the coastal swamp depobelt of the basin, to be a purely extensional stress tensor characterized by a maximum horizontal stress (SHmax) oriented NE-SW and a NW-SE principal extension direction. None of the three principal stresses was found to be truly vertical or horizontal.

Keywords: Stress regime; paleostress; inverse modeling.

**Corresponding author: E-mail: emmairoka@gmail.com;*

1. INTRODUCTION

Paleostress analysis concerns various methods of determining the orientations of the axes and relative magnitudes of the principal stresses of a regional stress tensor consistent with existing geologic structures. Several geologic structures can be used for paleostress reconstruction, these include fault populations, earthquake focal mechanism data, joint sets, dike sets, calcite twins, folds, kink bands, stylolites and fracture markings on joint surfaces [1]. The earliest application of a numerical method to fault-slip data inversion was done by [2]. However, there are at present numerous numerical algorithms (e.g. [3-12]) all of which are based on the relationship between stress and shear, introduced independently by [13] and [14] - although commonly referred to as the Wallace-Bott hypothesis. Numerical methods of paleostress analysis employ iterative approach to find a best-fit tensor with minimal angular deviation between the observed slip directions of faults and the theoretically determined directions of maximum shear stress on each fault plane.

Inverse modelling of geological fault-slip data, comprising of the strike and dip of fault planes, the orientations of their slip lines and the senses of shear on the fault planes, seeks to unravel the paleostress that produced the fault-striation data. It is simply the inverse application of Bott's [14] assumption which, in its direct form, states that slip on a fault plane occurs in the direction of the maximum resolved shear stress. Paleostress inversion methods do not yield all of the six parameters of the full stress tensor; rather they produce a reduced stress tensor characterized by four parameters: the orientations of the three principal stresses σ_1 (maximum principal stress), σ_2 (intermediate principal stress) and σ_3 (minimum principal stress) and the Stress Ratio $R = (\sigma_2 - \sigma_3)/(\sigma_1 - \sigma_3)$. The two additional parameters of the full stress tensor are the ratio of extreme principal stress magnitudes (σ_3/σ_1) and the lithostatic load, but these two cannot be determined from fault data only [15]. Also the reduced stress tensor does not contain information on the isotropic component of the stress tensor and therefore is identical with the deviatoric component of the tensor [16]. Hence, only relative magnitudes of the principal stresses can be obtained and not their absolute values.

3D seismic interpretation provides a means of deriving geometric information about subsurface structures that are not exposed on the Earth's surface. Structural interpretation of 3D seismic data provides useful geometric and kinematic information on subsurface faults from which paleostress tensors can be reconstructed where traditional outcrop based method, which uses fault striation measurements, is not possible. Numerous studies, both outcrop (e.g. [17]) and 3D seismic interpretations of faults [18-21], have shown that fault surfaces are not smooth but are made up of undulations. These corrugations are thought to result from hard linkage of small fault segments [22-24], or to reflect an inherent roughness of fault planes which form during initial failure [21].

Observations of fault surfaces at outcrop scale have shown that fault corrugations are parallel to the displacement directions of faults (e.g. [25]). However, as fault surfaces exhibit fractal-like property [26,27], corrugations observed on seismically interpreted faults are also parallel to slip directions on the faults, such that orientations of fault corrugations obtained by detailed seismic mapping can serve as kinematic indicators and therefore will yield paleostress information. This concept is supported by the works of [28,20,29,19,21]. The reason is simply that corrugations constitute asperities on a fault surface, and displacement on such a surface will require the least energy parallel to the axis of the undulation.

In this study, axes of fault surface corrugations - extracted from 3D seismic data acquired over a coastal field in the Western Niger Delta - are treated as movement indicators and consequently used for paleostress reconstruction. The objective is to constrain the orientations of the principal stresses and numerically define the tectonic regime of the upper Miocene (i.e. coastal swamp depobelt) in the Niger Delta, using the Stress Regime Index (R') of [30].

2. GEOLOGIC SETTING

The Niger Delta basin is a passive margin basin, located in the Gulf of Guinea, at the southern end of Nigeria, in West Africa. It is one of the largest deltas as well as one of the most prolific hydrocarbon provinces in the world [31-33]. It lies between latitudes 3^0 and 6^0N and longitudes 5^0 and 8^0E, overlying the coastal and oceanward part of a much larger and older tectonic feature, the Benue Trough [34]. Its northern boundary is delimited by the Benin Flank to the northwest, and to the northeast by the outcrops of Cretaceous sediments on the Abakiliki

Anticlinorium and by the Calabar Flank at its farthest northeast end [32]. Offshore Niger Delta is bounded by the Cameroon volcanic line at its southeastern end (Fig.1), the Okitipupa ridge to the west [35], and the two-kilometre sediment thickness contour or 4000-metres bathymetric contour in areas where sediment thickness is greater than 2 km to the south and southwest (Tuttle *et al*., 1999). The delta consists of a prism of siliciclastic sediments of the order of 12 km overall thickness [36] covering a total province area of 300,000km^2 [32].

Lithostratigraphy of the Tertiary section of the Niger delta consists of three formations distinguished mostly based on sand-shale ratios, and are considered to represent prograding deltaic facies. These formations, namely Akata, Agbada and Benin Formations, correspond to the prodelta, delta front and continental delta top facies respectively.

2.1 Tectonics

The continental margin in the Gulf of Guinea, along the west coast of Equatorial Africa, developed in the Early Cretaceous, during the opening of the Equatorial Atlantic Ocean [37-39]. Taphrogenic activities began in the south Atlantic and steadily progressed northward towards the Equatorial Atlantic region [40]. Rifting had advanced into seafloor spreading by the Aptian time (ca. 118 Ma.) in the vicinity of the Gulf of Guinea and Benue Trough [37]. According to [39] the Equatorial Atlantic was the locus of intersection of the central and south Atlantic rifts, and, therefore, it accommodated the differential opening of these oceans. This complicated its opening and resulted in the development of the Benue Trough and several other intracratonic rifts in West Africa and Northeast Brazil [38].

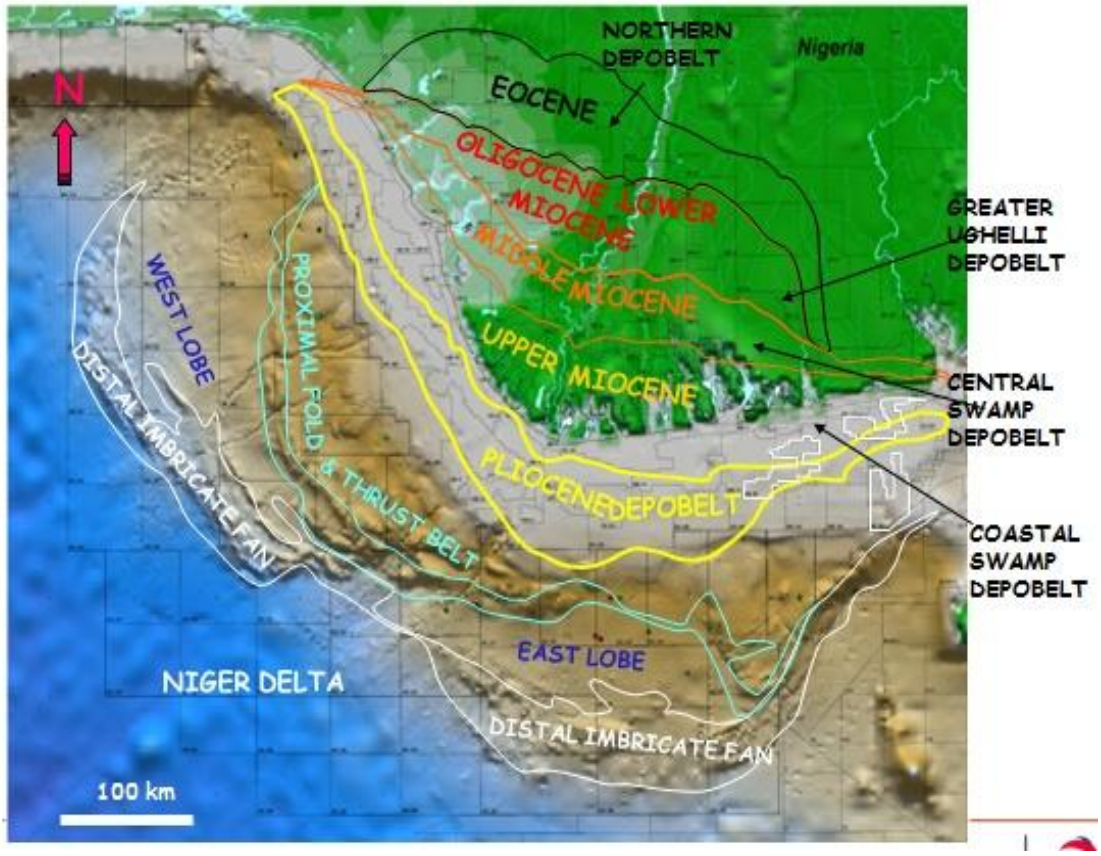

Fig. 1. Shaded relief and topographic map of the Niger Delta showing depobelts and their ages
(Source: TOTAL)

The Aptian–Albian time in the Equatorial Atlantic was characterized by the dominance of transtensional conditions, complicating the supposedly simple plate divergence by introducing shearing movements along the Benue trough arm of the Ridge-Ridge-Transform fault (RRF) triple junction that presently lies beneath the Niger Delta [41,37]. The Niger Delta basin overlies the coastal and offshore parts of the Benue Trough, which corresponds to the failed arm of a rift triple junction, in which the rifting ceased in the late Cretaceous. As such, its shape and internal structure are partly controlled by the continental extensions of the Equatorial Atlantic oceanic fracture zones (Fig.2), examples include the Chain and Charcot fracture zones (Fig.3), expressed as ridges and trenches in the deep Atlantic [32,42].

However, after rifting had ceased in the Benue Trough region and the Tertiary Niger Delta (which is the focus of this study) developed on the southern end of the Benue Trough by subsidence [43], gravity tectonism became the primary deformational process in the Tertiary Niger Delta. Mobility of the Akata shales (prodelta shales) triggered internal deformations, which occurred by way of gravity spreading of the sedimentary wedge [42], and created the growth faults that characterize the basin.

2.2 Structures

[44] divided the Cenozoic Niger Delta into three structural zones: an extensional zone (I) extending from onshore to the outer continental shelf and upper slope, an intermediate translational zone (II) beneath the continental slope and a compressional zone (III) beneath the lower continental slope and uppermost rise.

The extensional zone, also known as the fault-dominated zone [45] forms the most landward zone and it encompasses the coastal depobelt (Fig. 1) wherein the seismic data used for this study was acquired. Growth normal faults triggered by penecontemporaneous deformation of the delta front sediments (Agbada Fm) are the common structures here [34]. These synsedimentary faults are typical of basins undergoing gravity-driven deformation over a salt (e.g. Gulf of Mexico) or shale (e.g. Niger Delta) décollement layer. And slip on the regional listric growth normal faults generate rollover structures [47].

The intermediate translational zone of diapirs is characterized by passive, active, and reactive diapirism [48]. In this zone, shale ridges and massifs, shale overhangs, vertical mud diapirs (that form mud volcanoes at the seafloor) and interdiapir depocenters are known to occur [49]. The compressional zone of folds and thrust faults is the most distal of the structural belts, and defines a contractional zone in offshore Niger Delta. It extends from the lower continental slope to the upper part of the continental rise [44]. [42] further subdivided this zone into an inner fold and thrust belt, characterized by basinward facing thrust faults and associated folds and an outer fold and thrust belt in which both seaward- and landward-verging thrust faults and associated folds predominate.

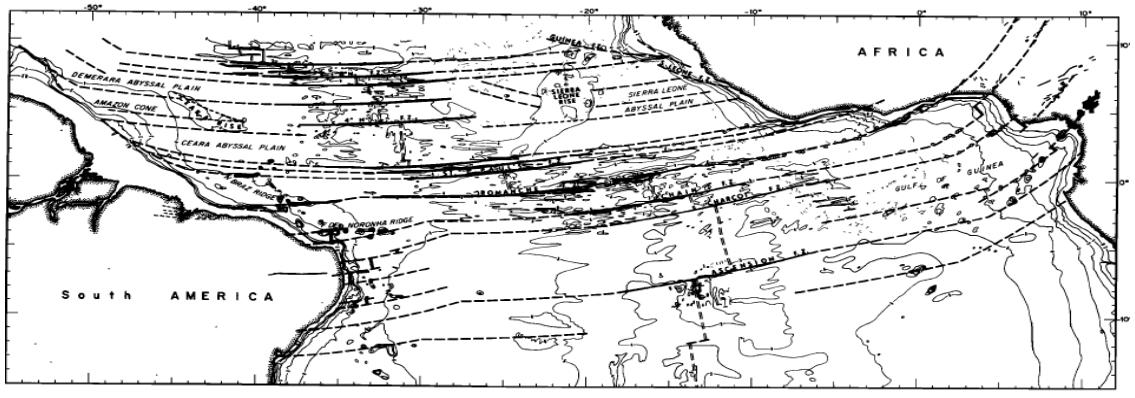

Fig. 2. Simplified bathymetric map of the Equatorial Atlantic Ocean showing the oceanic fracture zones and their continental extensions into the Benue Trough region in West Africa
Source: [46]

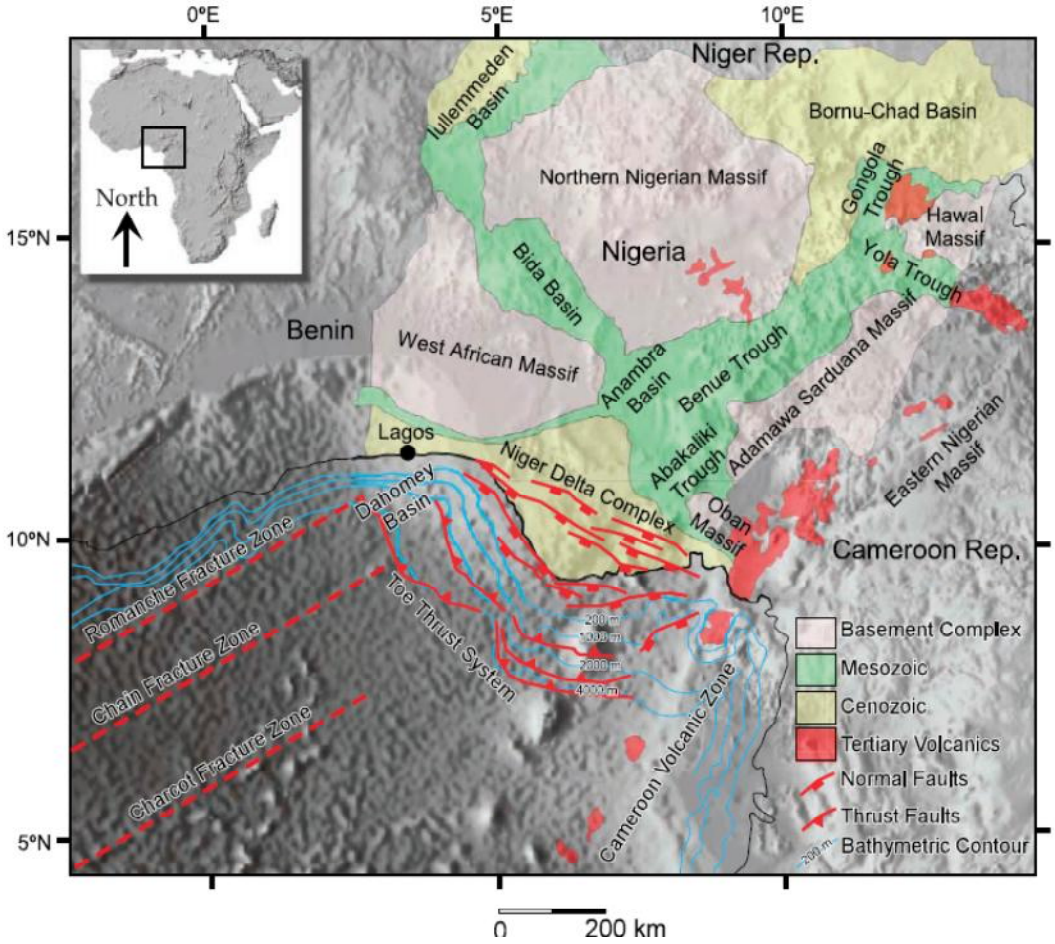

Fig. 3. Map of the Niger Delta region showing the main sedimentary basins and tectonic features

Source: [42]

3. MATERIALS AND METHODS

3.1 Materials

The data base for this study comprises of a post-stack time migrated three dimensional reflection seismic survey tied to four wells. The 3D seismic coverage provided by Shell Petroleum Development Company, Nigeria, amounts to 178 km^2 of the Coastal swamp depobelt, Niger Delta. Crosslines are oriented E-W and inlines are oriented N-S, with both lines spaced at 25 m interval. Hence the data has good spatial resolution. Fault mapping and geometric analysis was done using Petrel software version 2014 while paleostress inversion was carried out using Win-Tensor version 5.8.6.

3.2 Methods

Fault interpretation was done manually, with the fault sticks picked at intervals of 50 m and on sections (random lines) perpendicular to the local fault strike. Variance time slice intersections were used to constrain the fault mapping. The interpreted faults were modelled and validated from both geometrical and geological points of view. In all, 23 normal faults were geometrically and kinematically interpreted to obtain the requisite fault-slip data for use in the Win-Tensor program. The geometric analysis provided fault plane data (i.e. strike and dip of fault surfaces) while the kinematic data, comprising of slip directions and senses of movement on the faults, were respectively extracted from fault surface corrugations, accentuated by fault surface

asperity lineations, and cut-off points of seismic horizons on the fault surfaces.

Inversion of the fault slip data was carried out following the procedure described in [15], while the quality ranking scheme adopted is that of the world stress map project [50]. Prior to the iterative numerical modelling, the data were processed first, using the improved "Right Dihedron Method", to ascertain the range of possible orientations of σ_1 and σ_3. The result obtained, being only preliminary as the method does not verify the Coulomb criteria [15], was used as the starting stress tensor in the numerical modelling which was executed using the misfit function (F5) of the iterative "Rotational Optimization method".

4. RESULTS

4.1 Fault Interpretation

Orientation analysis of the fault population shows that the faults are not all clustered in a parallel arrangement, with respect to their strike, but have a somewhat girdle distribution with two pronounced clusters (fig.4). Approximately 60 percent of the faults comprise the larger cluster made up of a family of faults striking between 60^0 and 120^0; this array of faults can be called the E-W set. The other cluster, with a more restricted range of fault strikes (130^0 to 155^0), constitutes the SE-NW set. These faults make up the remaining 40 percent, and occur mostly on the south-western part of the field. This is unlike the E-W set which pervades the entire field. Measurements of dip magnitudes made on the fault planes indicate that the faults dip between 65^0 and 55^0 towards the south mostly.

Although the fault surfaces have corrugated patterns and undulating tip lines, it was necessary to extract asperity attribute from the surfaces in order to convert these features into a lineated pattern which is easier to measure. On each fault surface the mean direction of the asperity lineations was determined and used as the slip direction while its plunge magnitude was determined stereographically. As shown on Fig. 5, the asperity corridors plunge steeply, suggesting the preponderance of dip slip movements on the faults.

The result of the geometric interpretation of the faults and the kinematic information extracted from the asperity lineations, as shown on Fig. 6, constitute the input fault slip data that was subjected to numerical dynamic analysis to determine the nature of the paleostress tensor.

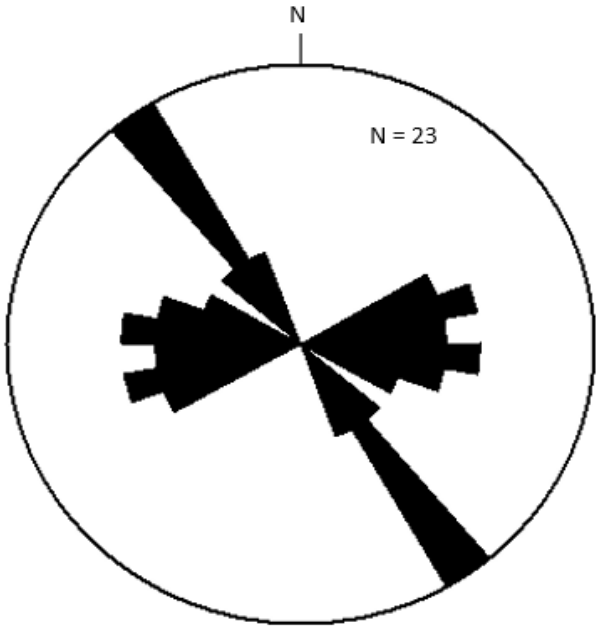

Fig. 4. Rosette presentation of the strike directions of the faults used for the dynamic analysis. Two sets of faults can be recognized based on the strike of the faults: an E-W set and a NW-SE set

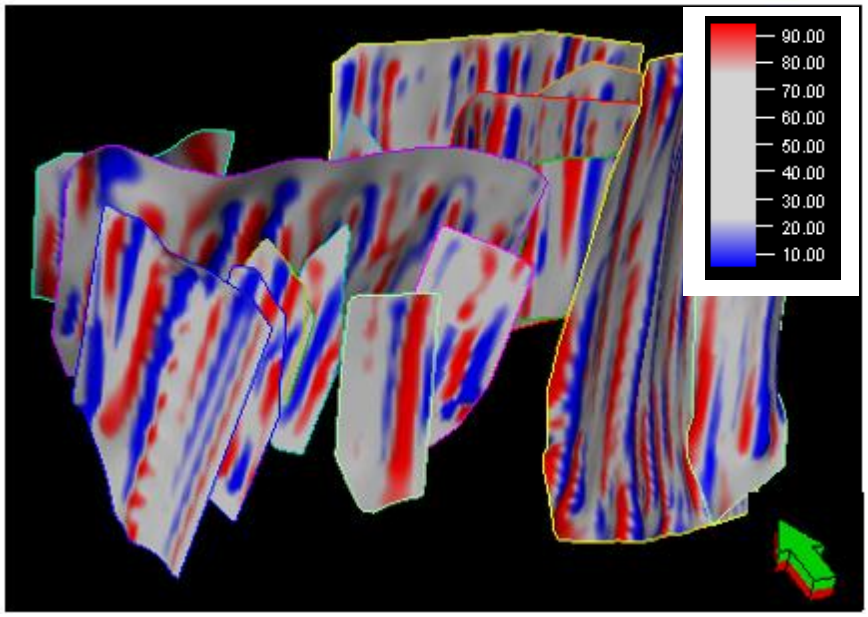

Fig. 5. Fault asperity attribute on the fault surfaces showing a linear pattern. Blue colour represents the concave part of the corrugation on the hanging wall side while red colour indicates convexity in the same direction. The faults are mostly southerly faults, dipping either southeast or southwest.

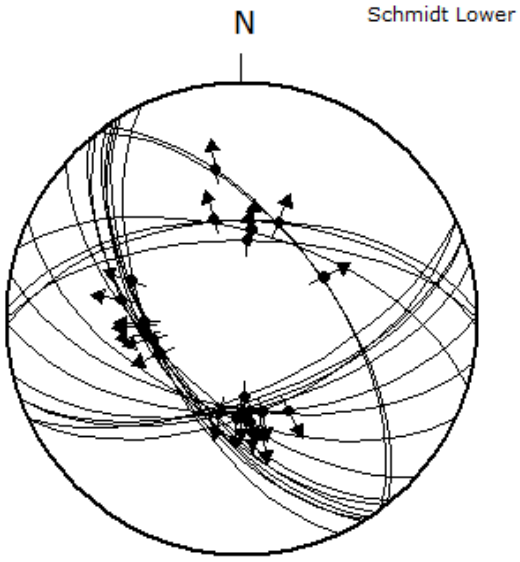

Fig. 6. Stereogram of the fault-slip data showing the dispositions of the fault planes and their associated kinematic indicators.

4.2 Dynamic Analysis

4.2.1 Right dihedron method

The improved right dihedron method is an upgraded numeric version of the graphical right dihedron method which was originally developed by [51]. [15] improved on the numeric version of the method to extend its applicability in paleostress analysis. Unlike the graphical version which is used mostly for focal mechanism studies, the improved numeric form, which is one

of the subroutines in the Win-tensor program, also estimates stress ratio R for a set of fault-slip data and runs a compatibility test on the data. It uses a counting deviation (CD) to determine if there are subsets within the data (for more information on the right dihedron method see [52,15].

Analysis of the fault-slip data using the improved right dihedron module of the Win-tensor program provided an initial estimate of a stress tensor which could account for the range of fault plane orientations, and directions and senses of slip extracted from the seismic data. The tensor is characterised by its principal stress axes and stress ratio R (Fig. 7). However, it has a very poor quality (E) owing to a subset of the data with anomalous counting deviations (i.e. CD > mean CD + 0.9σ).

Although this tensor was rejected on account of its quality, it served as a basis for separating the data into two subsets. As shown on Table 1, the emboldened data set, which have counting deviations higher than the threshold CD (i.e. mean CD + 0.9σ = 23.61) were consequently removed to form a different subset (subset 2).

The module was re-run after the removal of subset 2, characterised by anomalous CDs in the first run, and a new preliminary tensor of better quality (D) was obtained for subset 1(Fig. 8). The mean counting deviation dropped from 21% to 17.5% while the standard deviation of the CD dropped from 2.9 to 1.8. The improvement on the data quality can also be seen on the counting deviation histogram of Fig. 8 (bottom left of the diagram) when compared with that of Fig. 7.

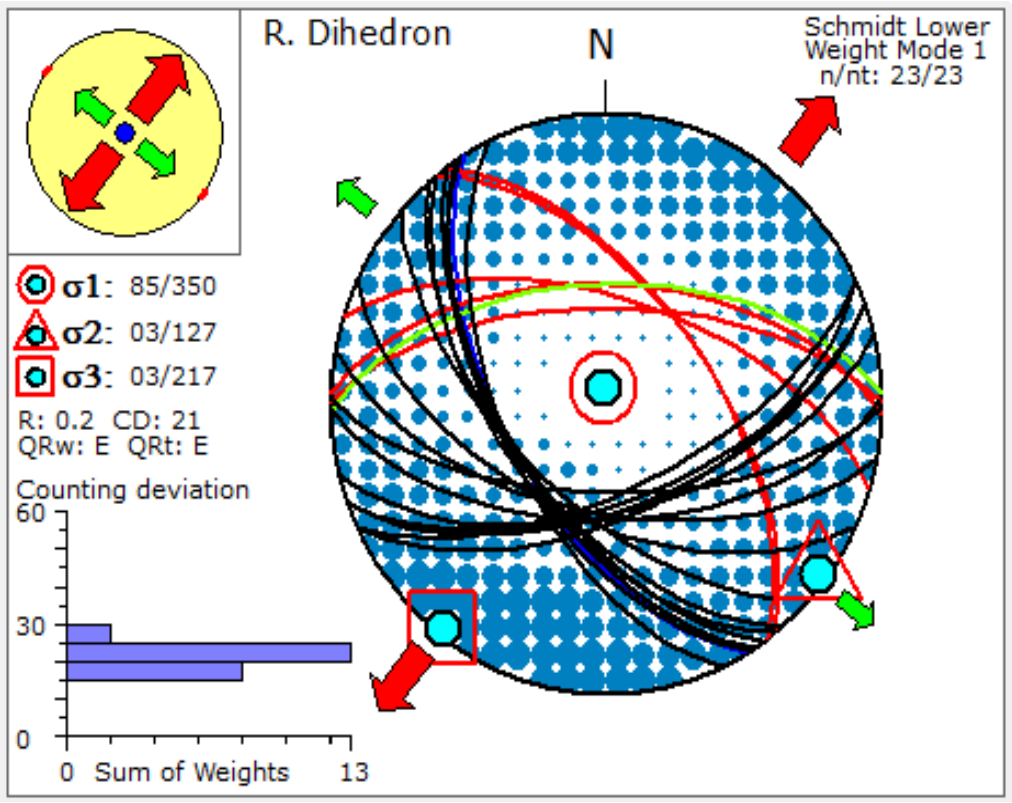

Fig. 7. Counting net and principal stress axes of a preliminary stress tensor generated for the entire fault-slip data using the improved right dihedron module. The data block shows the orientations of the principal stresses, stress ratio R, mean counting deviation (CD) and the quality rating of the tensor. Red and green fault traces make up the incompatible subset (i.e. high counting deviations) while black and blue traces constitute the compatible subset.

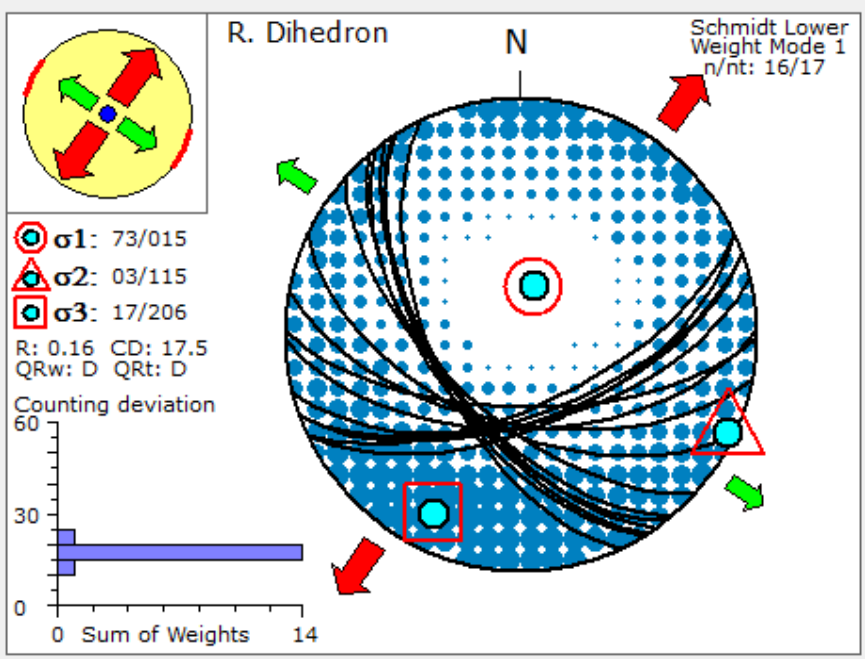

Fig. 8. Right dihedron solution after elimination of 6 data points. The tensor indicates a normal fault regime (subvertical σ_1) and its tensor quality rating is D. Note the counting deviation histogram and compare it with that of Fig. 7

4.3 Rotational Optimization

The rotational optimization module is an interactive and iterative paleostress inversion subroutine of the Win-tensor program that tests different stress tensors on a given population of fault-slip data to find a best-fit tensor that has the minimum value of the misfit function. The misfit function minimizes slip deviations (between the observed slip lines and computed shear stress directions) and the computed normal stress magnitudes on the fault planes using the reduced tensor being tested. At the same time, it maximizes the shear stress magnitudes and also verifies the Coulomb criterion for neoformed faults and Byerlee's law for reactivated faults [53,54]. Each run during the tests involves first the adjustment of the stress axes through rotations, then the stress ratio *R*. The process is iterated several times until the tensor is stabilized, at which point further rotations of the stress axes or adjustment of the stress ratio do not improve the results [15]. Using Means' method [55], for each tensor tested the direction, sense and magnitude of the shear stress acting on each fault plane as well as the magnitude of the related normal stress and the characteristic dihedral angle and the friction angle were computed.

Prior to the separation of the fault population into two subsets a rotational optimization of the entire fault-sip data was carried out in order to be able to observe the effect the separation would have on the paleostress inversion. As shown on Fig. 9, the best-fit reduced stress tensor (optimized solution) for the entire data population is a normal fault stress regime. Its stress ratio (R = 0.15) lies within the range of radial extension, whereas the horizontal principal stress axes suggest the main direction of extension to be N - S. The weighted mean value of the composite misfit function F5 is 6.9, while the tensor quality rating based on the world stress map project (QRw) is C.

There are data points with slip deviations (α) greater than twenty-five degrees, as presented in table 2, suggesting that the data population does not belong to a single homogeneous stress field [52] as is commonly assumed in all paleostress analysis [21]. The data points with high slip deviations also have anomalous values of the misfit function (F5). Moreover, using the standard of [15] in which case a slip deviation (α) ≤ 30^0 is accepted as compatible with the theoretically computed shear, there is still incompatible data in the optimized result. All these are indications that the best-fit reduced stress tensor found for

the fault-slip data cannot satisfactorily account for the range of fault plane orientations and their associated directions and senses of slip.

4.3.1 Optimized solution for subset 1

Optimization of the main subset (i.e. subset 1) after the removal of those with high counting deviations, as highlighted in the right dihedron result, yielded the reduced paleostress tensor shown below (fig. 10). Table 3 presents the input data and the parameters of the optimized tensor for each fault-slip data in subset 1.

5. DISCUSSION

5.1 Antithetic Faults

At the data input stage, care was taken to ensure that the faults were differentiated based on their directions of dip. Synthetic faults, which dominate the data set were assigned input values of 1 while the antithetic faults were designated as input 2. This enabled easy monitoring of the behaviour of the synthetic and antithetic faults at all stages of the numerical dynamic analysis. From the result of the right dihedron method, it is quite obvious that the incompatible data, characterized by high counting deviations, are the antithetic faults with northerly directions of dip (see table 1). These faults have counting deviations greater than 23.61 which is the threshold value defined for the counting deviations. As such, the separation of the antithetic faults from the synthetic faults, based on the improved right dihedron result, is geologically valid since the faults do not belong to the same family with respect to their directions of dip.

Analysis of the rotational optimization result (Table 2) shows that these antithetic faults cannot be separated from the synthetic faults based on slip deviation α (alpha) and the value of the misfit function F5, which are the

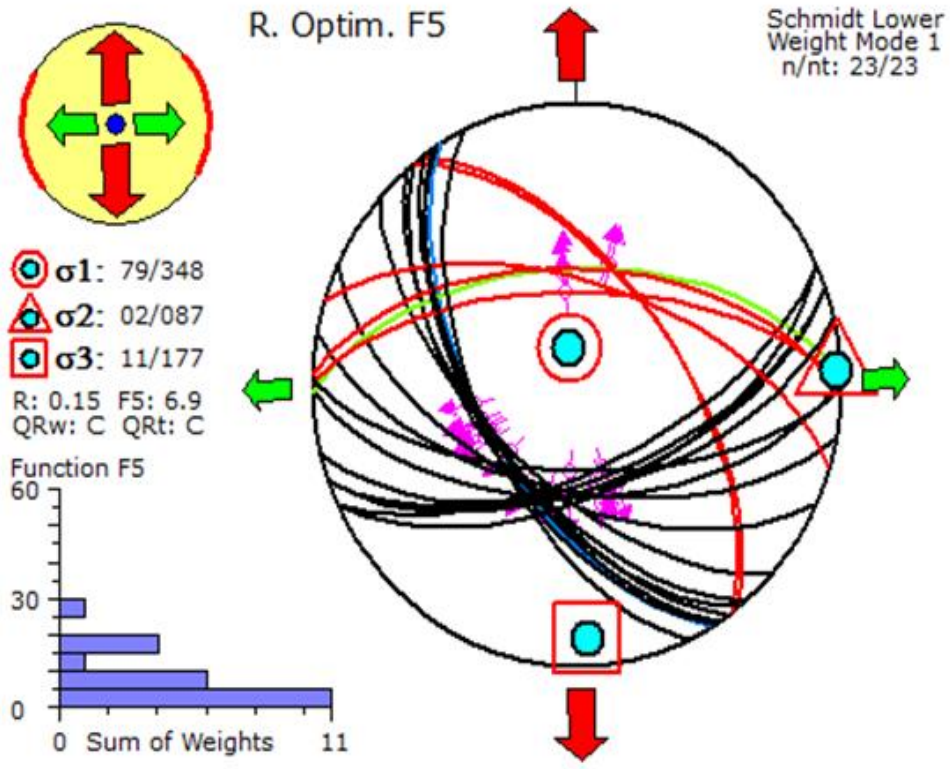

Fig. 9. Rotational optimization solution for the entire fault-slip data. The tensor is extensional. Its stress ratio R indicates that there is also significant extension in the E-W direction, although the main extension direction is N-S

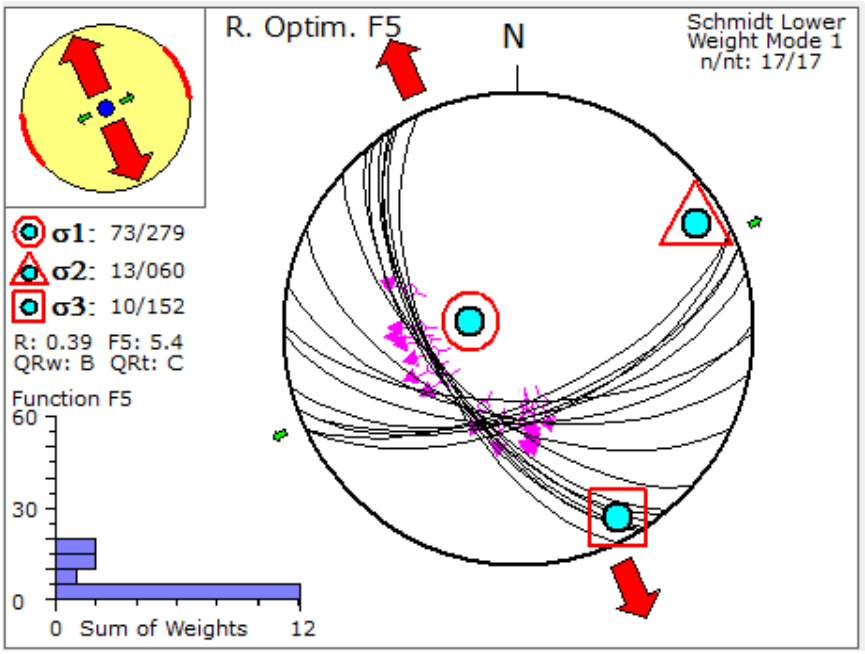

Fig. 10. Final optimized solution for the field studied. The tensor has a better quality rating (B) based on the world stress map (QRw), and its slip deviation histogram shows no data points with anomalous slip deviation values

commonly used indices of incompatibility. However, a closer examination of Table 2 shows that the antithetic faults can be differentiated from the synthetic faults based on their phi (Ø) values, shear sense, normal stress (N-mag) and shear stress (T-mag) magnitudes. These faults have higher Ø values compared to the synthetic faults, and dihedral angles (2θ) computed from their Ø values average 27^0 whereas the synthetics have average 2θ value of 41^0. Considering that the value of 2θ decreases with decreasing depth [56], this observation is in agreement with the view of [27] that antithetic faults are minor faults that are restricted to the upper (shallower) part of the main faults. Also, the magnitudes of the normal and shear stresses (N-mag and T-mag in Table 2, columns 11 & 12) computed from the reduced stress tensor further support the occurrence of these antithetic faults at shallower levels, being characterised by low magnitudes. Lastly, shear sense computed from the tensor (Table 2, column 7) show all the faults to be largely dip-slip faults with only small lateral components of slip. For the synthetic faults their lateral slip components have dextral sense of movement, whereas the antithetic faults have lateral-slip components with sinistral sense of movement.

5.2 Paleostress Tensor and Tectonic Stress Regime

As has already been emphasized, the paleostress tensor is a reduced stress tensor characterised by four parameters: the orientations of the three principal stresses (σ_1, σ_2, and σ_3) and the stress ratio R. Fig. 10 shows the final optimized solution, which is the best-fit tensor for the upper Miocene (coastal swamp depobelt) of the Niger Delta. The tensor is characterised by a subvertical maximum principal stress axis σ_1 indicating a normal fault regime. Plunge direction of the intermediate principal stress axis σ_2 (N 60^0 E) for the reduced tensor obtained lies subparallel to the strike of the regional fault (N65^0E) bounding the studied field while the trend of the principal extension axis (σ_3), being perpendicular to this direction, parallels the dip direction of the regional bounding fault. This observation corroborates the finding of [30] that the principal extension axis (σ_3) tends to be perpendicular to the major border fault trace. Besides, the true maximum horizontal stress (SHmax = N 66^0 E) for the tensor is actually parallel to the strike of the regional fault, while the actual minimum horizontal stress (Shmin = S 24^0 E) or true horizontal extension direction is parallel to the dip

azimuth of the regional fault (155^0). Non-coincidence of the maximum and minimum horizontal stresses with horizontal principal stresses is a consequence of the vertical principal stress not being truly vertical [57].

For the stress ratio R, which indicates the shape of the stress ellipsoid [52] and carries relative magnitude information about the principal stresses [16], the best-fit value for the tensor is 0.39. This means that on a magnitude scale where σ_1 is fixed at 100 and σ_3 at zero, σ_2 would have a magnitude of 39 [15] for the tensor. [30] used the concept of stress regime index R' to numerically define the type of stress tensor on a numerical scale that ranges between 0 and 3. It is computed from the stress shape ratio R, knowing which of the three principal stresses is vertical. Based on this scheme R' = R for extensional regimes and R' of 0.39 falls within the range of pure extension (i.e. σ_1 vertical and $0.25 < R < 0.75$). Hence the upper Miocene of the Niger Delta, in the Coastal depobelt, was deformed under a purely extensional stress regime, with a NW – SE horizontal direction of extension.

From the Mohr-Coulomb point of view, most of the movements (slips) occurred on pre-existing planes of weakness as indicated on Table 3. These slip surfaces identified as RF (i.e. reactivated faults) in Table 3 are characterized by Mohr distances greater than 10 while the neoformed (NF) slip surfaces have Mohr-dist values less than 10. This is because neotectonic faults follow the Mohr-Coulomb criterion for fault initiation [1] and therefore lie at, or near the tangent point of the maximum friction line (Coulomb failure envelop) on the Mohr circle (Fig. 11) whereas faults activated on pre-existing planes of weakness follow the frictional sliding criterion [15] and lie inside the Mohr circle, farther away from the failure envelop (some may lie very close to the minimum friction line).

The existence of such planes of weakness in the sedimentary fabric of the Agbada formation, in the Coastal swamp depobelt studied, could explain the absence of conjugate faults within the field. The reason is that conjugate fault sets are neoformed faults, which are usually suppressed where weakness planes occur [11].

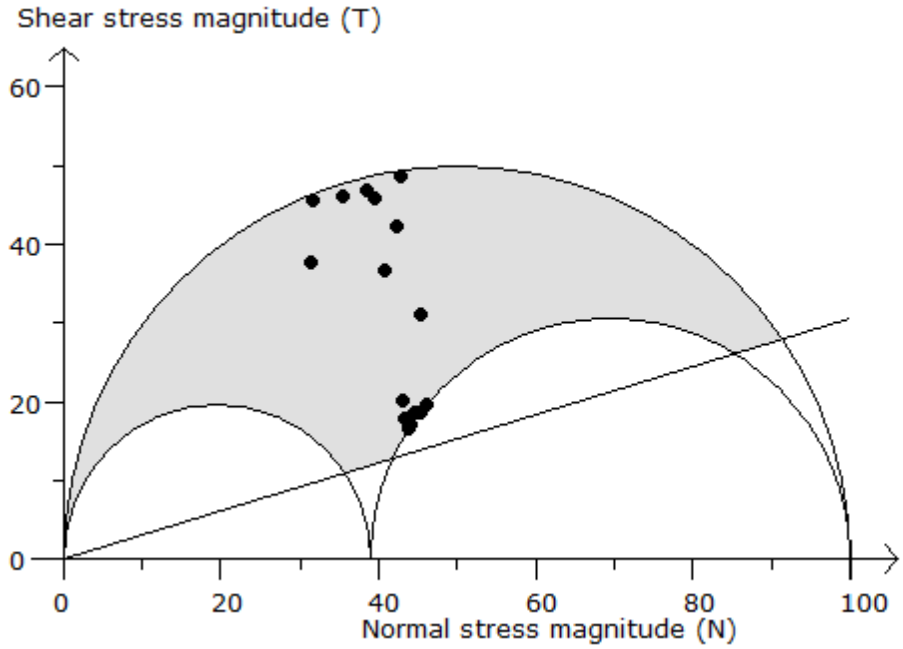

Fig. 11. Mohr circle pattern for the synthetic faults based on the optimized tensor characteristics. There are four neoformed faults aligned close to the major circle, the rest of the faults were apparently activated on pre-existing weakness planes

Table 1. Right dihedron result for the entire fault-slip data

ID	Plane	Line	Sense	CD	P incl	p azim	b incl	b azim	t incl	t azim	Shmax	Shmin	R'	Regime
akos-08	63/360	63/004	ND	26.81	87	153	02	271	03	001	091	001	0.5	NF
akos-09	59/052	58/063	ND	25.71	83	128	05	325	02	235	145	055	0.5	NF
akos-17	60/239	49/289	ND	24.47	65	338	26	165	03	074	163	073	0.5	NF
akos-04	60/017	59/006	NS	24.36	83	290	05	104	01	194	104	014	0.5	NF
akos-01	59/054	36/350	NS	23.9	50	313	39	115	09	212	125	035	0.5	NS
akos-10	56/002	54/344	NS	23.66	79	296	09	086	05	177	088	178	0.5	NF
akos-21	58/232	47/279	ND	23.37	64	325	25	159	06	066	154	064	0.5	NF
akos-11	56/358	54/021	ND	22.52	79	073	11	276	04	185	094	004	0.5	NF
akos-14	61/235	56/268	ND	21.42	74	332	15	154	01	064	154	064	0.5	NF
akos-13	60/230	55/266	ND	21.36	74	326	17	150	01	060	150	060	0.5	NF
akos-15	59/245	58/257	ND	21.27	83	323	05	158	01	068	158	068	0.5	NF
akos-16	58/238	56/261	ND	20.56	79	321	11	155	02	064	154	064	0.5	NF
akos-19	62/222	49/170	NS	20.37	63	120	27	296	02	027	117	027	0.5	NF
akos-22	65/155	63/178	ND	20.3	79	276	09	069	04	160	071	161	0.5	NF
akos-18	60/237	59/247	ND	20.1	83	322	04	150	01	060	150	060	0.5	NF
akos-06	62/160	57/193	ND	18.85	74	260	15	078	00	168	078	168	0.5	NF
akos-23	65/181	65/179	NS	18.7	85	009	01	271	05	181	091	001	0.5	NF
akos-20	58/155	55/183	ND	18.64	77	241	13	073	03	343	072	162	0.5	NF
akos-07	60/160	58/180	ND	18.09	80	251	09	075	01	345	075	165	0.5	NF
akos-12	57/179	54/153	NS	17.93	77	099	12	261	04	352	083	173	0.5	NF
akos-05	59/166	58/175	ND	17.13	83	237	04	078	02	348	078	168	0.5	NF
akos-03	57/205	54/175	NS	16.94	77	120	14	285	03	016	107	017	0.5	NF
akos-02	59/191	57/168	NS	16.72	80	103	11	275	01	005	095	005	0.5	NF

Table 2. Rotational optimization result for the entire fault population prior to separation into subsets

Input data							Optimization results (resolved stress)						
ID	**Plane**	**Line**	**Sense**	**Input**	**Shear**	**Sense**	**Alpha**	**Phi**	**M-Dist**	**Nmag**	**Tmag**	**F5**	**Type**
akos-17	60/239	49/289	ND	1	60/246	ND	**26.8**	46.3	10.8	38.4	40.2	18.8	R F
akos-23	65/181	65/179	NS	1	65/184	ND	1.9	56	2.5	31.2	46.3	0.1	N F
akos-8	63/360	63/004	ND	2	63/355	NS	3.9	72	16.5	9.6	29.4	0.4	R F
akos-5	59/166	58/175	ND	1	59/170	ND	2.8	49.4	13.5	41.9	49	0.4	R F
akos-15	59/245	58/257	ND	1	59/255	ND	1.2	45.3	11.8	39.2	39.6	0.5	R F
akos-18	60/237	59/247	ND	1	60/243	ND	2.2	46.5	10.7	38.5	40.6	0.6	R F
akos-4	60/017	59/006	NS	2	58/356	NS	5.2	66.6	9.3	14.8	34.3	0.7	N F
akos-22	65/155	63/178	ND	1	65/162	ND	7.1	54.1	3.8	32.7	45.2	1.4	N F
akos-10	56/002	54/344	NS	2	56/357	NS	7.6	64.9	4.2	18	38.4	1.5	N F
akos-7	60/160	58/180	ND	1	60/165	ND	8.2	49.9	12	40.5	48.2	2	R F
akos-16	58/238	56/261	ND	1	58/245	ND	8.8	45.1	13	41.3	41.5	2.5	R F
akos-2	59/191	57/168	NS	1	59/192	ND	13	49.9	12.6	41	48.7	4.6	R F
akos-20	58/155	55/183	ND	1	58/159	ND	13.6	47.6	15.6	44.2	48.3	5.1	R F
akos-11	56/358	54/021	ND	2	56/356	NS	14.2	65	4.4	17.8	38.3	5.2	N F
akos-6	62/160	57/193	ND	1	62/165	ND	14.7	51.9	8.6	37.2	47.4	5.7	N F
akos-14	61/235	56/268	ND	1	61/240	ND	15.5	47.4	9.6	37.2	40.4	6.6	N F
akos-12	57/179	54/153	NS	1	57/182	ND	16.4	48	16.5	44.8	49.7	7.3	R F
akos-3	57/205	54/175	NS	1	57/206	ND	17.8	47.2	15.4	44.1	47.7	8.5	R F
akos-13	60/230	55/266	ND	1	60/233	ND	18	47.3	10.5	38.8	42	8.7	R F
akos-9	59/052	58/063	ND	2	54/018	NS	25.1	54.2	6.3	26.6	37	16.3	N F
akos-01	59/054	36/350	NS	2	54/020	NS	27.3	53.5	6.6	27.4	37	19.2	N F
akos-21	58/232	47/279	ND	1	58/237	ND	27.2	45.6	13.1	41.7	42.6	19.4	R F
akos-19	62/222	49/170	NS	1	62/222	NX	31.3	49.8	7.7	36.1	42.6	25.1	N F

Table 3. Final optimized solution for the fault-slip data comprising subset 1

Input data					Optimization result						
ID	**Plane**	**Line**	**Shear**	**Sense**	**Alpha (α)**	**Phi (Ø)**	**M-dist**	**Nmag**	**Tmag**	**F5**	**Type**
akos-21	58/232	47/279	57/245	ND	22.7	23.1	30.8	46	19.6	16	R F
akos-19	62/222	49/170	61/204	NS	22.2	25.2	28.8	43.1	20.2	15	R F
akos-15	59/245	58/257	50/289	ND	20.5	22.4	31.1	43.3	17.8	13.5	R F
akos-13	60/230	55/266	60/235	ND	17	22.6	31.1	44.7	18.6	10.2	R F
akos-17	60/239	49/289	56/271	ND	13.1	21	32.2	43.9	16.9	7.3	R F
akos-12	57/179	54/153	57/175	NS	13	44.9	13.9	42.4	42.2	4.9	R F
akos-18	60/237	59/247	57/263	ND	8.5	21.1	32.1	44.2	17.1	4.7	R F
akos-14	61/235	56/268	60/254	ND	8.2	20.7	32.4	43.8	16.5	4.6	R F
akos-6	62/160	57/193	61/172	ND	11.5	52.5	6.6	35.4	46.1	3.6	N F
akos-3	57/205	54/175	56/190	NS	8.6	34.5	21.7	45.3	31.1	3.4	R F
akos-16	58/238	56/261	55/266	ND	3.2	22.4	31.3	45.3	18.7	3	R F
akos-23	65/181	65/179	64/162	NS	7.5	50.1	8	31.4	37.6	1.7	N F
akos-20	58/155	55/183	57/172	ND	6.3	48.5	14.4	42.9	48.5	1.3	R F
akos-2	59/191	57/168	58/176	NS	4.2	41.9	14.8	40.9	36.7	1.2	R F
akos-7	60/160	58/180	59/172	ND	4.2	50.5	9.9	38.6	46.9	0.6	N F
akos-5	59/166	58/175	59/173	ND	1.5	49.2	10.7	39.5	45.7	0.3	R F
akos-22	65/155	63/178	64/173	ND	2.2	55.4	2.6	31.5	45.6	0.2	N F

Shear refers to the orientation of the maximum shear stress computed for each fault plane based on the modelled tensor and the orientation of the fault plane; ND stands for normal slip with small dextral component; NS stands for normal slip with small sinistral component; alpha is the angular deviation between the observed slip and the computed direction of maximum shear stress on the fault plane; Ø is the friction angle; M-dist refers to the distance of each data point from the tangential point when plotted on the Mohr circle using Tmag and Nmag; Tmag is the magnitude of the shear stress on the fault plane; Nmag is the magnitude of the normal stress opposing the shear stress; F5 is a composite misfit function; NF stands for neoformed fault and; RF stands for reactivated fault.

5.3 Effect of Antithetic Faults on Dynamic Analysis

When the 6 antithetic faults of subset 2 were subjected to rotational optimization, the resultant optimized tensor showed some semblance to that obtained for the synthetic faults. The stress regime index (R' = 0.33) is similar to that for the optimized solution obtained using the synthetic faults (R' = 0.39), indicating pure extensional stress regime for both tensors. Also the orientation of the subvertical principal stress σ_1 is similar for both subsets (78/273 for subset 2 and 73/279 for subset 1). However, these tensors differ greatly in their horizontal principal stress orientations. For subset 2 (antithetic faults) principal extension direction is NE-SW (021^0) with SHmax acting in the direction of 110^0 while for subset 1 (synthetic faults) extension direction is SE-NW (152^0) with SHmax trending 066^0.

It is interesting to find that principal extension direction (177^0) and SHmax orientation (086^0) characterising the initial optimized tensor solution for the entire fault population (i.e. combined synthetic and antithetic faults) shown in Fig. 9 are approximately, mean values obtainable by merging tensor solutions for subsets 1 and 2. Considering the ratio of the number of faults in each subset (6:17), it is clear that antithetic faults exert strong influence on horizontal principal stress axes orientation of paleostress tensors obtained by numerical dynamic analysis. In addition, they have a sense of shear that is opposite to the externally imposed shear and also arise due to a secondary stress field developing around the main fault when movement occurs on a listric fault [1,27]. Therefore antithetic faults should not be used for paleostress reconstruction.

6. CONCLUSIONS

1. Faults in the coastal swamp depobelt are basically dip slip faults with only small lateral components of displacement.
2. The improved right dihedron method is a better module for separating a group of faults into subsets than the rotation optimization module, as it can recognize geometric inconsistency (e.g. opposing directions of dip).
3. Gravity tectonics which deformed the Upper Miocene Agbada Fm, in the coastal swamp depobelt of the Niger Delta, was characterised by a pure extensional stress regime, with a NW-SE horizontal direction of extension. The horizontal principal stresses do not coincide with the actual SHmax and Shmin due to the subvertical character of the maximum principal stress.
4. Activation of existing planes of weakness can explain why conjugate fault sets are uncommon in the field studied.
5. Antithetic faults exert strong influence on the horizontal stress axes of reduced stress tensors obtained by numerical dynamic analysis, and should, therefore, not be included.

COMPETING INTERESTS

Author has declared that no competing interests exist.

REFERENCES

1. Schimmrich SH. Evaluation of computational methods of paleostress analysis using fault-striation data. Unpublished Masters Thesis, Department of Geological sciences, State University of New York, Albany, U.S.A; 1991.
2. Carey E, Brunier B. Analyse théorique et numérique d'un modèle méchanique élémentaire appliqué à l 'étude d'une population de failles. Comptes Rendus Hebdomadaires de L'Académie des Sciences France, Série D. 1974;279:891-894.
3. Angelier J. Determination of the mean principal directions of stresses for a given fault population. Tectonophysics. 1979;56: T17-T26.
4. Etchecopar A, Vasseur G, Daignieres M. An inverse problem in microtectonics for the determination of stress tensors from fault striation analysis. Journal of Structural Geology. 1981;3:51-56.
5. Angelier J, Tarantola A, Valette B, Manoussis S. Inversion of field data in fault tectonics to obtain the regional stress. I. Single phase fault populations: A new method of computing the stress tensor. Geophysical Journal of the Royal Astronomical Society. 1982;69:607-621.
6. Vasseur G, Etchecopar A, Philip H. Stress state inferred from multiple focal mechanisms. Annales Geophysicæ. 1983;1:291-298.
7. Angelier J. Tectonic analysis of fault slip data set. Journal of Geophysical Research. 1984;89:5835-5848.

8. Gephart JW, Forsyth DW. An improved method for determining the regional stress tensor using earth quake focal mechanism data: Application to the San Fernando earthquake sequence. Journal of Geophysical Research. 1984;89:9305-9320.
9. Michael AJ. Determination of stress from slip data: Faults and folds. Journal of Geophysical Research. 1984;89:11517-11526.
10. Reches Z. Determination of the tectonic stress tensor from slip along faults that obey the Coulomb yield condition. Tectonics. 1987;6:849-861.
11. Angelier J. From orientation to magnitudes in paleostress determinations using fault slip data. Journal of Structural Geology. 1989;11:37-50.
12. Delvaux D. The tensor program for paleostress reconstruction: Examples from the east African and the Baikal rift zones. In: Terra Abstracts. Abstract supplement 1993;1. to Terra Nova, 5, 216.
13. Wallace RE. Geometry of shearing stress and relation to faulting. Journal of Geology. 1951;59:118-130.
14. Bott MHP. The mechanism of oblique-slip faulting. Geological Magazine. 1959;96: 109-117.
15. Delvaux D, Sperner B. New aspects of tectonic stress inversion with reference to the tensor program. In D. A. Nieuwland (Ed.), New Insights into Structural Interpretation and Modelling. Geological Society, London, Special Publications. 2003;212:75-100.
16. Kaymakci N. Kinematic development and paleostress analysis of the Denizli Basin (Western Turkey): Implications of spatial variation of relative paleostress magnitudes and orientations. Journal of Asian Earth Sciences. 2006;27:207-222.
17. Peacock DCP, Zhang X. Field examples and numerical modelling of oversteps and bends along normal faults in cross section. Tectonophysics. 1994;234:147–167.
18. Mansfield CS, Cartwright JA. High resolution fault displacement mapping from three-dimensional seismic data: evidence for dip linkage during fault growth. Journal of Structural Geology. 1996;18(2/3):249–203.
19. Lohr T, Krawczyk C, Oncken O, Tanner D. Evolution of a fault surface from 3D attribute analysis and displacement measurements. Journal of Structural Geology. 2008;30(6):690–700.
20. Gartrell AP, Lisk M. Potential new method for paleostress estimation by combining three-dimensional fault restoration and fault slip inversion techniques: first test on the Skua Field, Timor Sea. In P. Boult, & J. Kaldi, (Eds.), Evaluating fault and cap rock seals. AAPG Hedberg Series. 2005;2:23–26.
21. Van Gent HW, Back S, Urai JL, Kukla PA, Reicherter K. Paleostresses of the Groningen area, the Netherlands – results of a seismic based structural reconstruction. Tectonophysics; 2008. DOI:10.1016/j.tecto.2008.09.038.
22. Peacock DCP. Propagation, interaction and linkage in normal fault systems. Earth-Science Reviews, 2002;58:121–142.
23. Marchal D, Guiraud M, Rives T. Geometric and morphologic evolution of normal fault planes and traces from 2D to 4D data. Journal of Structural Geology. 2003;25:135–158.
24. Baudon C, Cartwright J. The kinematics of reactivation of normal faults using high resolution throw mapping. Journal of Structural Geology. 2008;30:1072–1084.
25. Hancock PL, Barka AA. Kinematic indicators on active normal faults in western Turkey. Journal of Structural Geology. 1987;9(5/6):573-584.
26. Scholz CH. The mechanics of earthquakes and faulting. Cambridge: Cambridge University Press. 1990;439.
27. Mandl G. Faulting In brittle rocks: An introduction to the mechanics of tectonic faults. Berlin: Springer-Verlag. 2000;434.
28. Needham DT, Yielding G, Freeman B. Analysis of fault geometry and displacement patterns. In P.G. Buchanan, & D.A. Nieuland (Eds.), Modern Developments in Structural Interpretation, Validation, and Modeling. Geological Society Special Publication. 1996;99:189–199.
29. Lohr T. Seismic and sub-seismic deformation on different scales in the NW German Basin. PhD thesis, Freie Universität Berlin; 2007.
30. Delvaux D, Moeys R, Stapel G, Petit C, Levi K, Miroshnichenko A, Ruzhich V, San'kov V. Paleostress reconstructions and geodynamics of the Baikal region, Central Asia. Part II: Cenozoic rifting. Tectonophysics. I997;282:1-38.

31. Doust H, Omatsola E. Niger Delta. In J.D. Edwards & P.A. Santogrossi (Eds.), Divergent/passive margin basins, AAPG Memoir. 1990;48:201–238.
32. Tuttle MLW, Charpentier RR, Brownfield ME. The Niger Delta petroleum system: Niger Delta province, Nigeria, Cameroon, and Equatorial Guinea, Africa. USGS Open-File Report. 1999;99-50-H.
33. Jermannaud P, Rouby D, Robin C, Nalpas T, Guillocheau F, Raillard S. Plio-Pleistocene sequence stratigraphic architecture of the eastern Niger Delta: A record of eustasy and aridification of Africa. Marine & Petroleum Geology. 2010;27:810-821.
34. Reijers TJA, Petters SW, Nwajide CS. The Niger Delta Basin. In R.C. Selley (Ed.), African Basins: Sedimentary basins of the world,3. Amsterdam: Elsevier Science. 1997;151-172.
35. Nwajide CS. Geology of Nigeria's Sedimentary Basins. Lagos: CSS Bookshops Ltd. 2013;565.
36. Knox GJ, Omatsola EM. Development of the Cenozoic Niger delta in terms of the "escalator regression" model and impact on hydrocarbon distribution. In proceedings of the KNGMS Symposium on Coastal Lowlands, Geology and Geotechnology. Dortrecht: Klower Academic Publishers. 1989;181–202.
37. Briggs SE, Cartwright J, Davies RJ. Crustal structure of the deepwater west Niger Delta passive margin from the interpretation of seismic reflection data. Marine and Petroleum Geology. 2009;26:936–950.
38. Matos RMD. Tectonic evolution of the Equatorial South Atlantic. In W. Mohriak & M. Talwani (Eds.), Atlantic Rifts and Continental Margins. Geophysical Monograph. 2000;115:331–354.
39. Fairhead JD, Binks RM. Differential opening of the Central and South Atlantic oceans and the opening of the West African rift system. Tectonophysics. 1991;187(1–3):191–203.
40. Nurnberg D, Muller RD. The tectonic evolution of the South Atlantic from Late Jurassic to present. Tectonophysics. 1991;191(1–2):27–53.
41. Fairhead JD. Late Mesozoic rifting in Africa. In W. Manspeizer (Ed.), Triassic-Jurassic Rifting-Continental Breakup and the origin of the Atlantic Ocean and Passive Margins. Developments in Geotechnics, 22, Amsterdam: Elsevier. 1988;821–831.
42. Corredor F, Shaw JH, Bilotti F. Structural styles in the deep-water fold and thrust belts of the Niger Delta. American Association of Petroleum Geologists Bulletin. 2005;89:753–780.
43. Reijers TJA. Stratigraphy and sedimentology of the Niger Delta. Geologos. 2011;17(3):133-162.
44. Damuth JE. Neogene gravity tectonics and depositional processes on the deep Niger Delta continental margin. Marine and Petroleum Geology. 1994;11(3):320–346.
45. Wu S, Bally AW. Slope tectonics and contrasts of structural styles of salt and shale tectonics of the northern Gulf of Mexico with shale tectonics of offshore Nigeria in Gulf of Guinea. In W. Mohriak, & M. Talwani (Eds.), Atlantic Rifts and Continental Margins. American Geophysical Union Geophysical Monograph Series. 2000;151–172.
46. Sibuet JC, Mascle J. Plate kinematic implications of Atlantic Equatorial Fracture zone trends. Journal of Geophysical Research. 1978;83(B7):3401–3421.
47. Jackson CAL, Rotevatn A. 3D seismic analysis of the structure and evolution of a salt-influenced normal fault zone: A test of competing fault growth models. Journal of Structural Geology. 2013;54:215–234.
48. Morley CK, Guerin G. Comparison of gravity driven deformation styles and behavior associated with mobile shales and salt. Tectonics. 1996;15(6):1154–1170.
49. Graue K. Mud volcanoes in deepwater Nigeria. Marine and Petroleum Geology. 2000;17:959– 974.
50. Sperner B, Muller B, Heidbach O, Delvaux D, Reinecker J, Fuchs K. Tectonic stress in the Earth's crust: Advances in the World Stress Map project. In D.A. Nieuwland (Ed.), New Insights into Structural Interpretation and Modelling. Geological Society, London, Special Publications. 2003;212:101-116.
51. Angelier J, Mechler P. Sur une methode graphique de recherche des contraintes principales egalement utilisable en tectonique et en seismologie: La methode des diedres droits. Bulletin de la Societe Geologique de France. 1977;7(19):1309-1318.
52. Ramsay GJ, Lisle R. The Techniques of Modern Structural Geology volume 3:

Applications of Continuum Mechanics Structural Geology. Amsterdam: Elsevier Academic Press. 2000;360.
53. Delvaux D, Moeys R, Stapel G, Melnikov A, Ermikov V. Paleostress reconstructions and geodynamics of the Baikal region, Central Asia. Part I: Paleozoic and Mesozoic pre-rift evolution. Tectono-physics. 1995;252:61-101.
54. Macheyeki AS, Delvaux D, Batist M, Mruma A. Fault kinematics and tectonic stress in the seismically active Manyara–Dodoma Rift segment in Central Tanzania – Implications for the East African Rift. Journal of African Earth Sciences. 2008;51:163-188.
55. Means WD. A construction for shear stress on a generally oriented plane. Journal of Structural Geology. 1989;11:625-627.
56. Oden MI, Asinya AE, Udinmwen E. The schist enclaves of Oban massif, southeastern Nigeria: Consistency of dihedral angle and other natural physical and mechanical properties. Journal of Geography, Environment and Earth Science International. 2017;9(1):1-13.
57. Lund B, Townend J. Calculating horizontal stress orientations with full or partial knowledge of the tectonic stress tensor. Geophysics Journal International. 2007; 170:1328-1335.

Peer-review history:
The peer review history for this paper can be accessed here:
http://www.sciencedomain.org/review-history/26860